Linear, Nonlinear Optical Susceptibilities and the Hyperpolarizability of Borate LiBaB9O15 Single-Crystal: Theory and Experiment.

7 AUTHORS, INCLUDING:

Ali H Reshak
University of West Bohemia

477 PUBLICATIONS **3,425** CITATIONS

SEE PROFILE

Sushil Auluck
Indian Institute of Technology Kanpur

313 PUBLICATIONS **3,092** CITATIONS

SEE PROFILE

H. Kamarudin
Universiti Malaysia Perlis

365 PUBLICATIONS **1,164** CITATIONS

SEE PROFILE

Iwan V Kityk
Czestochowa University of Technology

961 PUBLICATIONS **7,943** CITATIONS

SEE PROFILE

Linear and Nonlinear Optical Susceptibilities and the Hyperpolarizability of Borate LiBaB$_9$O$_{15}$ Single-Crystal: Theory and Experiment

A. H. Reshak,*[,†,‡] Xuean Chen,[§] S. Auluck,[¶] H. Kamarudin,[‡] Jan Chyský,[□] A. Wojciechowski,[⊥] and I. V. Kityk[⊥,△]

[†]Institute of Complex Systems, FFPW, CENAKVA, University of South Bohemia in Ceske Budejovice, Nove Hrady 37333, Czech Republic

[‡]Center of Excellence Geopolymer and Green Technology, School of Material Engineering, University Malaysia Perlis, 01007 Kangar, Perlis, Malaysia

[§]College of Materials Science and Engineering, Beijing University of Technology, Ping Le Yuan 100, Beijing 100124, PR China

[⊥]Electrical Engineering Department, Technical University of Czestochowa, Al.Armii Krajowej 17/19, Czestochowa, Poland

[¶]Council of Scientific Research, National Physical Laboratory, Dr. K. S. Krishnan Marg, New Delhi 110012, India

[□]Department of Instrumentation and Control Engineering Faculty of Mechanical Engineering, Czech Technical University in Prague, Prague, Czech Republic

[△]Physical Department, Eastern European University, Al. Voli 6, Lutsk, Ukraine

S *Supporting Information*

ABSTRACT: The single-crystal borate LiBaB$_9$O$_{15}$ was synthesized by a high-temperature solution reaction and structurally determined by the single-crystal X-ray diffraction technique. It crystallizes in the noncentrosymmetric space group $R3c$ and features a three-dimensional $_\infty^3[B_9O_{15}]^{3-}$ anionic framework, with infinite channels in which the Li$^+$ and Ba^{2+} cations are located. The linear optical properties were investigated experimentally in terms of the absorption spectrum, which reveals an optical gap of 5.17 eV. In addition we have calculated the linear optical properties using state-of-the-art all-electron full potential linearized augmented plane wave method. The nonlinear optical susceptibilities, namely, the second harmonic generation and the hyperpolarizability of the single-crystal borate LiBaB$_9$O$_{15}$ are calculated and evaluated at a static limit and at λ = 1064 nm. The calculation shows there exists three second-order nonlinear optical susceptiblities tensors components. We present measurements of the IR spectra in the range 500−2000 cm^{-1}, and the second harmonic generation was performed using a Quantel 15 ns Nd:YAG laser operating at 1064 nm.
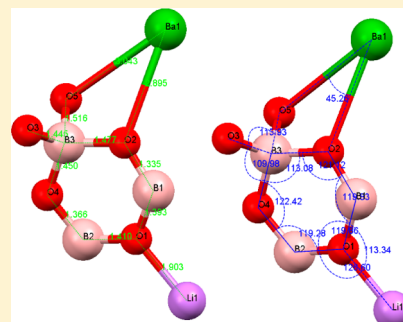
1. INTRODUCTION

In the past thirty years, alkali- and alkaline earth-metal borates have been widely investigated because they have important practical applications in the field of laser technology.[1−3] For example, LiB$_3$O$_5$[4] and β-BaB$_2$O$_4$[5] are well-known nonlinear optical (NLO) crystals. It is reasonable to believe that new NLO materials might also be expected in the ternary borates incorporating both the alkali-metal element Li and the alkaline earth-metal element Ba. On the basis of this idea, several ternary lithium barium borates, LiBaBO$_3$, LiBa$_2$B$_5$O$_{10}$, and LiBaB$_9$O$_{15}$, were synthesized, among which the former two compounds crystallize in the centrosymmetric space groups, $P2_1/c$ and $P2_1/m$, respectively; thus, no NLO effects are observed. The crystal structure of LiBaBO$_3$ consists of isolated BO$_3$ groups,[6] while the structure of LiBa$_2$B$_5$O$_{10}$ contains a one-dimensional (1D) chain of the complex borate anion [B$_5$O$_8$O$_{4/2}$]$^{5-}$ formed by three BO$_3$ triangles ($\triangle$) and two BO$_4$ tetrahedra (T), which can be viewed as one triborate

[B$_3$O$_4$O$_{4/2}$]$^-$ group bonded to two BO$_3$ triangles; this leads to a fundamental building block with the shorthand notation 5: ∞^1[(3 : $\triangle$+2T) + 2 $\triangle$].[7] For the boron-richest phase, LiBaB$_9$O$_{15}$, the structural data indicate 3D networks built up from triborate [B$_3$O$_7$]$^{5-}$ groups; however, the data published in the literature are contradictory: Penin et al.[8] proposed the noncentrosymmetric $R3c$ structure, while Pushcharovskii et al.[9] suggested the centrosymmetric $R\bar{3}c$ group. In the course of our investigation of new borate NLO materials, we have obtained single crystals of LiBaB$_9$O$_{15}$. Our X-ray structural analysis (CSD No. 426537) has confirmed the structural model proposed by Penin et al.[8] The present study is aimed to measure the linear and nonlinear optical susceptibilities using a Nd:YAG laser operating at 1064 nm. In addition we will calculate the linear and nonlinear

optical susceptibilities of the LiBaB$_9$O$_{15}$ crystal by using the full potential linear augmented plane wave (FP-LAPW) method which has proven to be one of the most accurate methods for computing the electronic structure of solids within the density functional theory (DFT) approach. To the best of our knowledge, no experimental data and first principle calculations on the linear and nonlinear optical properties of LiBaB$_9$O$_{15}$ has so far appeared in the literature. Therefore, we thought it would be worthwhile to perform detailed calculations of the linear and nonlinear optical properties of LiBaB$_9$O$_{15}$.

2. EXPERIMENTAL SECTION

2.1. Syntheses, X-ray Crystallography, and Spectrum Properties. The single crystal LiBaB$_9$O$_{15}$ was synthesized from a high-temperature solution reaction using analytical grade reagents: 2.9997 g of BaCO$_3$, 1.2374 g of ZnO, 6.1097 g of H$_3$BO$_3$, and 0.8429 g of Li$_2$CO$_3$ (BaCO$_3$/ZnO/H$_3$BO$_3$/Li$_2$CO$_3$ molar ratio = 4:4:26:3). The sample was introduced into a 40 mL Pt crucible, which was placed in the center of a vertical, programmable temperature furnace. The samples were heated at 830 °C for one week and then allowed to gradually cool to 810 °C at a rate of 1.0 °C/h, to 600 °C at 5.0 °C/h, and finally to room temperature at 20 °C/h. The colorless, transparent, prismatic crystals of LiBaB$_9$O$_{15}$ were obtained in about 40% yield. The byproduct accompanying LiBaB$_9$O$_{15}$ was a mixture of unknown borates. Note that Zn was not incorporated into the final structure, although ZnO was used as a starting material. In the synthesis of the title compound, a stoichiometric mixture of Li$_2$CO$_3$, BaCO$_3$, and H$_3$BO$_3$ did not melt when heated until 850 °C. The addition of ZnO in a molar ratio of BaCO$_3$/ZnO/H$_3$BO$_3$/Li$_2$CO$_3$ = 4:4:26:3 causes a significant lowering of the melting point of this system to about 810 °C, which is favorable for the crystal growth. A single-phase polycrystalline sample of LiBaB$_9$O$_{15}$ was obtained by the direct reaction of a stoichiometric mixture of Li$_2$CO$_3$, BaCO$_3$, and H$_3$BO$_3$ at 600 °C for four weeks with several intermediate grindings. Powder X-ray analysis using the monochromatized Cu Kα radiation of a Bruker D8 Advance diffractometer has confirmed the phase purity.

A colorless crystal with the approximate dimensions of 0.20 mm × 0.10 mm × 0.10 mm was put on an automated Rigaku AFC7R four-circle diffractometer equipped with a graphite-monochromatic Mo Kα radiation (λ = 0.71073 Å). The data were collected at room temperature by using an ω-2θ scan mode in the range of $3.21 \leq \theta \leq 29.96°$. A total of 1100 reflections were collected, of which 588 were independent (R_{int} = 0.0219), and 541 reflections with $I > 2\sigma(I)$ were considered to be observed. The absorption correction based on the empirical phase-shifting interferometric scan technique was applied, and the crystal structure was solved by direct methods and refined in the SHELX-97 system[10] by full-matrix least-squares techniques on F_o^2. Details of the crystal parameters, data collection, structure refinements, the atomic coordinates and the equivalent isotropic displacement parameters are summarized in the Supporting Information (CSD No. 426537).

Figure 1 displays the crystal structure of the title compound. Observe that the basic structural unit in LiBaB$_9$O$_{15}$ is a [B$_3$O$_7$]$^{5-}$ group that consists of one BO$_4$ tetrahedron (T) and two BO$_3$ triangles ($\triangle$) condensed into a six-membered ring via the common O atoms. In an isolated form, the [B$_3$O$_7$]$^{5-}$ group contains three bridging O atoms and four terminal O atoms. Each [B$_3$O$_7$]$^{5-}$ group is linked to four other similar groups through sharing all of the terminal O atoms to form a

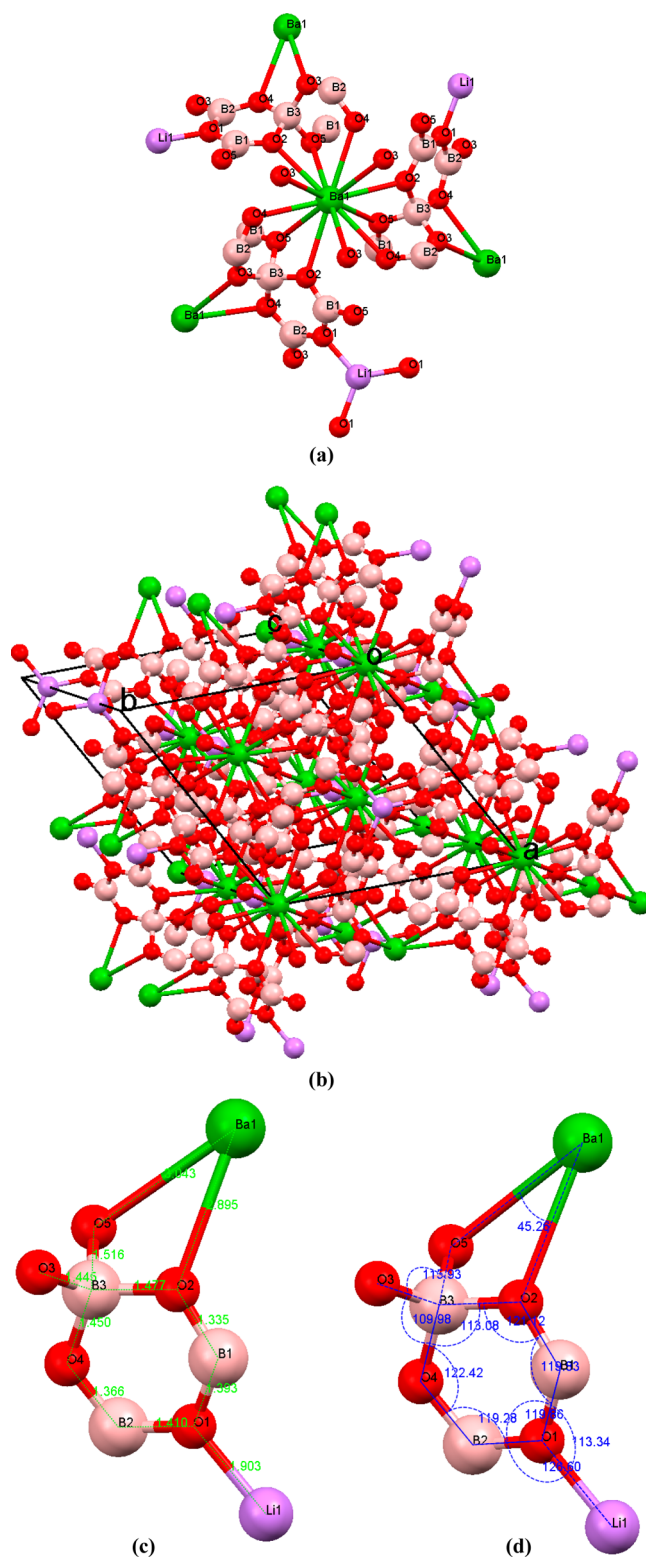**Figure 1.** The crystal structure of LiBaB$_9$O$_{15}$.

three-dimensional (3D) $^3_\infty$[B$_9$O$_{15}$]$^{3-}$ network, which can be written as 3: ∞^3[(3 : 2$\triangle$+T)] according to the definition given by Christ and Clark[11] and Heller.[12] The open channels in the 3D network are alternately filled by the Li$^+$ and Ba^{2+} cations.

2.2. Infrared Spectral Measurements. The sample of about 5 mg of LiBaB$_9$O$_{15}$ was finely ground with 100 mg of dry

KBr. The collected powder was placed in a stainless steel IR holder and pressed to form a semitransparent pellet that was used for IR collection. The UV−vis diffuse reflectance spectra were collected using a Shimadzu UV-3101PC double-beam, double-monochromator spectrophotometer over the spectral range of 200−1000 nm at room temperature. $BaSO_4$ powder (100% reflectance) was used as a reference. The reflectance spectra were converted to absorbance using the Kubelka−Munk equation, $F(R) = (1 − R)^2/(2R)$, where R represents the reflectance. The minima in the second-derivative curves of the Kubelka−Munk function are taken as a position of the absorption bands. The emission spectrum was measured at room temperature using the Fluorolog-Tau-3 (ISA-USA) fluorescence spectrometer equipped with a laser light of 325 nm wavelength.

For further confirmation of the coordination surroundings of the B atoms, the IR spectrum of $LiBaB_9O_{15}$ was collected and presented in Figure 2. Following this figure one can see that the

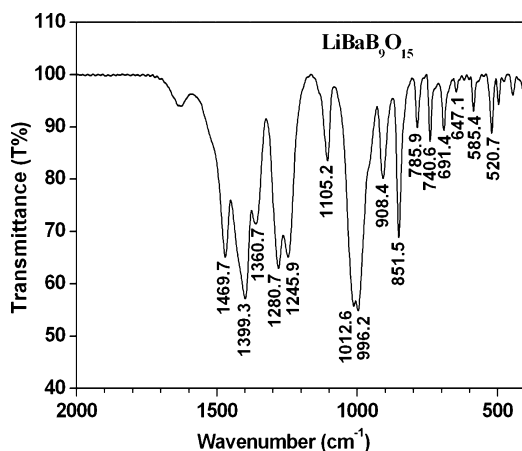**Figure 2.** Infrared spectra of $LiBaB_9O_{15}$.

BO_3 asymmetric stretching vibrations (ν_{as}) were seen between 1469.7 and 1245.9 cm^{-1}, while the BO_4 asymmetric stretching vibrations (ν_{as}) were observed at 1105.2−996.2 cm^{-1}. The absorption bands in the frequency range between 908.4 and 851.5 cm^{-1} may be associated with both of the BO_3 and BO_4 symmetric stretching modes, while the absorption bands occurring below 785.9 cm^{-1} can be assigned to both the BO_3 and BO_4 bending modes. The BO_3 group is distorted from the ideal D_{3h} symmetry, and the BO_4 is distorted from the T_d symmetry in $LiBaB_9O_{15}$. This removes the degeneracy of the IR active vibrations resulting in the band split and also allows the nonactive vibrations $\nu_s(BO_3)$ and $\nu_s(BO_4)$ to absorb energy in the IR region. Therefore, the IR spectrum confirms the existence of trigonally and tetrahedrally coordinated boron atoms, which is consistent with the results obtained from the crystallographic data.

The reflectance spectra of $LiBaB_9O_{15}$ were converted to absorbance using the Kubelka−Munk function, as illustrated in Figure 3. Following this figure one can observe a strong absorption band which peaks at around 200 nm (6.20 eV), whereas there is no absorption above 400 nm. These observed values were consistent with the transparency of the material in the range of visible wavelengths. The absorption edge of the UV−vis diffuse reflectance spectrum occurs at 240 nm, from which the optical band gap is estimated to be roughly 5.17 eV, which is consistent with the observed color. Also it is consistent
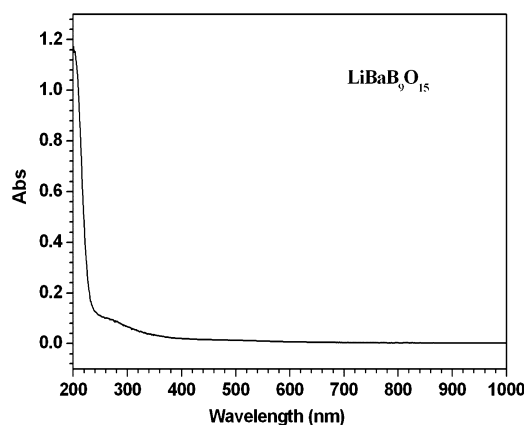

Figure 3. Optical absorption spectrum of $LiBaB_9O_{15}$.

with the fact that $LiBaB_9O_{15}$ has an even number of electrons and is predicted to be a semiconductor. In addition, the emission spectrum of $LiBaB_9O_{15}$ excited by laser light of wavelength 325 nm is presented in Figure 4. Observe that there

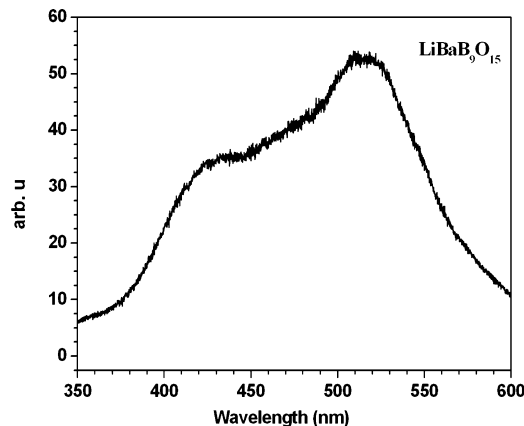**Figure 4.** Emission spectrum of $LiBaB_9O_{15}$.

exists one emission region situated between 400 and 550 nm, with the emitted main peak localized at around 515 nm (2.41 eV) and one shoulder at around 430 nm (2.88 eV). Since the emission energy is significantly less than the optical absorption edge of 5.17 eV, we can deduce that the emitted fluorescence probably originates from the defects or excitons.

2.3. Second Harmonic Generation (SHG) Measurement. The nonlinear optical experiment of the second harmonic generation was performed using a Quantel 15 ns Nd:YAG laser operating at 1064 nm. The power density was successively varied up to 1.2 GW/cm^2, and the registration was performed by the Hamamatsu photomultiplier connected with doubled filters (532 nm before the photomultiplier and 1064 nm before the samples). The statistic includes up to 200 points for each power density. The Tektronix oscilloscope allows the exclusion of the long time scattering with respect to the pure SHG. To perform the comparison with the experiment we have performed studies of the microcrystalites embedded into the polymer matrix that were additionally oriented by an external direct current (DC) electric field. Generally the experiment was performed with respect to the reference crystal BiB_3O_6. The experiment was similar to that described in ref 13, oriented in the external DC electric fields. We have performed the experiment for the input/output polarizations corresponding

to the tensor components d_{31} and d_{33}. We have found that for the 1064 nm Nd:YAG nanosecond laser pulses the corresponding values were 0.45 pm/V for d_{31} and 1.21 pm/V for d_{33} (the dominant component). These values are listed in Table 2 in comparison with the theoretical predictions.

3. THEORETICAL CALCULATIONS

Using our measured X-ray data (see the Supporting Information, CSD No. 426537) we have started the calculations by minimizing the forces (1 mRy/au) acting on each atom to optimize the atomic positions. Once the forces are minimized in this construction one can then find the self-consistent density at these positions by turning off the relaxations and driving the system to self-consistency. From the relaxed geometry the linear and nonlinear optical susceptibilities were calculated and compared with the experimental results. The state-of-the-art all-electron full potential linearized augmented plane wave (FP-LAPW) method within the framework of the WIEN2K code[14] was used. This is an implementation of the DFT[15] with different possible approximations for the exchange correlation (XC) potentials. In this calculation the XC potential is described by two approximations, the local density approximation (LDA) of Ceperley–Alder (CA)[16] and the generalized gradient approximation (GGA) of Perdew–Becke–Ernzerhof (PBE),[17] which are based on the XC energy optimization to calculate the total energy. The potential and charge density in the muffin-tin (MT) spheres are expanded in spherical harmonics with $l_{max} = 8$ and nonspherical components up to $l_{max} = 6$. The self-consistent calculations are converged since the total energy of the system is stable within 10^{-5} Ry. Self-consistency is obtained using 200 $\vec{k}$ points in the irreducible Brillouin zone (IBZ). The linear and nonlinear optical susceptibilities were calculated using 1200 k-points in the IBZ.

4. RESULTS AND DISCUSSION

4.1. Salient Feature of the Electronic Band Structures. Now we can use our calculated band structure to indicate the transitions which are responsible for the major structures of the optical dielectric function dispersions. The electronic band structure of $LiBaB_9O_{15}$, calculated from the optimized geometry, shows that the valence band maxima (VBM) and the conduction band minima (CBM) are located at the center of the BZ, resulting in a direct wide band gap semiconductor. The value of the direct gap is 5.01 eV using the LDA, while using the GGA shifts the CBM dramatically toward higher energies leading to opening a bigger gap of about 5.11 eV. Thus the GGA gives a better energy band gap in comparison to our measured value (5.17 eV). Figure 5 illustrates the calculated electronic band structures along with the optical transitions depicted on a generic band structure.

4.2. Linear Optical Dispersion. As the borate $LiBaB_9O_{15}$ crystallizes in the trigonal space group $R3c$ (Supporting Information, CSD No. 426537), the dielectric tensor has three components corresponding to the electric field $\vec{E}$ along the a, b, and c crystallographic axes. These are $\varepsilon^{xx}(\omega)$, $\varepsilon^{yy}(\omega)$, and $\varepsilon^{zz}(\omega)$, respectively. It is well known that for trigonal symmetry $\varepsilon^{xx}(\omega) = \varepsilon^{yy}(\omega)$; thus, the symmetry allows only two components corresponding to the electric field $\vec{E}$ parallel or perpendicular to the c-axis. Therefore the complex tensor components are $\varepsilon^{xx}(\omega) = \varepsilon_2^{\perp}(\omega)$ and $\varepsilon^{zz}(\omega) = \varepsilon_2^{\parallel}(\omega)$. The imaginary part of these complex components are $\varepsilon_2^{xx}(\omega)$ and
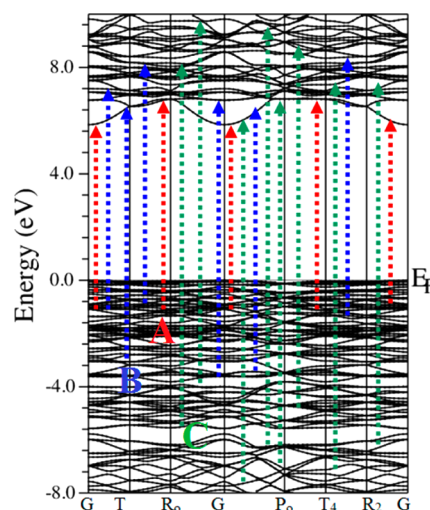

Figure 5. The calculated band structures (a) LDA and (b) GGA. The optical transitions are depicted on a generic band structure.

$\varepsilon_2^{zz}(\omega)$. The imaginary parts of the optical function's dispersion completely define the linear optical properties. These are shown in Figure 6a,b.

To demonstrate the effect of XC potentials on the linear optical properties the $\varepsilon_2^{average}(\omega)$ was calculated using the LDA and GGA as illustrated in Figure 6a. Notice that the GGA shifts the spectrum toward higher energy by around 0.1 eV. Broadening is taken to be 0.1 eV, which is traditional for borate crystals and typical of the experimental accuracy.[18−20] All the optical properties are scissors corrected by 0.1 eV; more details about the scissors correction are given in ref 21. Basically this increases the separation between the valence and conduction bands rigidly by 0.06 eV. The scissors correction is the difference between the calculated and measured energy gap. It is a consequence of the fact that the density functional theory calculations usually underestimate the energy gaps with respect to the experimental ones. A very simple way to overcome this drawback is to use the scissors correction factors, which merely brings the calculated energy gap close to the experimental gap. From Figure 6b, one can see that the edges of the optical absorptions (fundamental absorption edges) for $\varepsilon_2^{xx}(\omega)$ and $\varepsilon_2^{zz}(\omega)$ are located at 5.17 eV. These edges of optical absorption give the threshold for the direct optical transitions between the VBM and CBM. The two components display two principal peaks situated around 9.0 and 12.5 eV, respectively. Three significant humps are situated on the top of the first principle peak, with an insignificant hump located on the left-hand side of the first principle peak. A considerable anisotropy between these two components of the dielectric function's dispersions was observed. It is well known that a crystal that shows a considerable anisotropy in the linear optical susceptibilities favors an enhanced phase, matching the conditions for the second harmonic generation (SHG) and the optical parametric oscillation (OPO). To identify the spectral peaks in the linear optical spectra, we considered the optical transition matrix elements. We have used our calculated band structure to indicate the transitions which are responsible for the major structure of the principal components $\varepsilon_2^{xx}(\omega)$ and $\varepsilon_2^{zz}(\omega)$. These transitions are labeled according to the spectral peak positions in Figure 6b. For simplicity, we have labeled the transitions in Figures 5 and 6b as A, B, and C. The A transitions are responsible for the structures of $\varepsilon_2^{xx}(\omega)$ and $\varepsilon_2^{zz}(\omega)$ in the
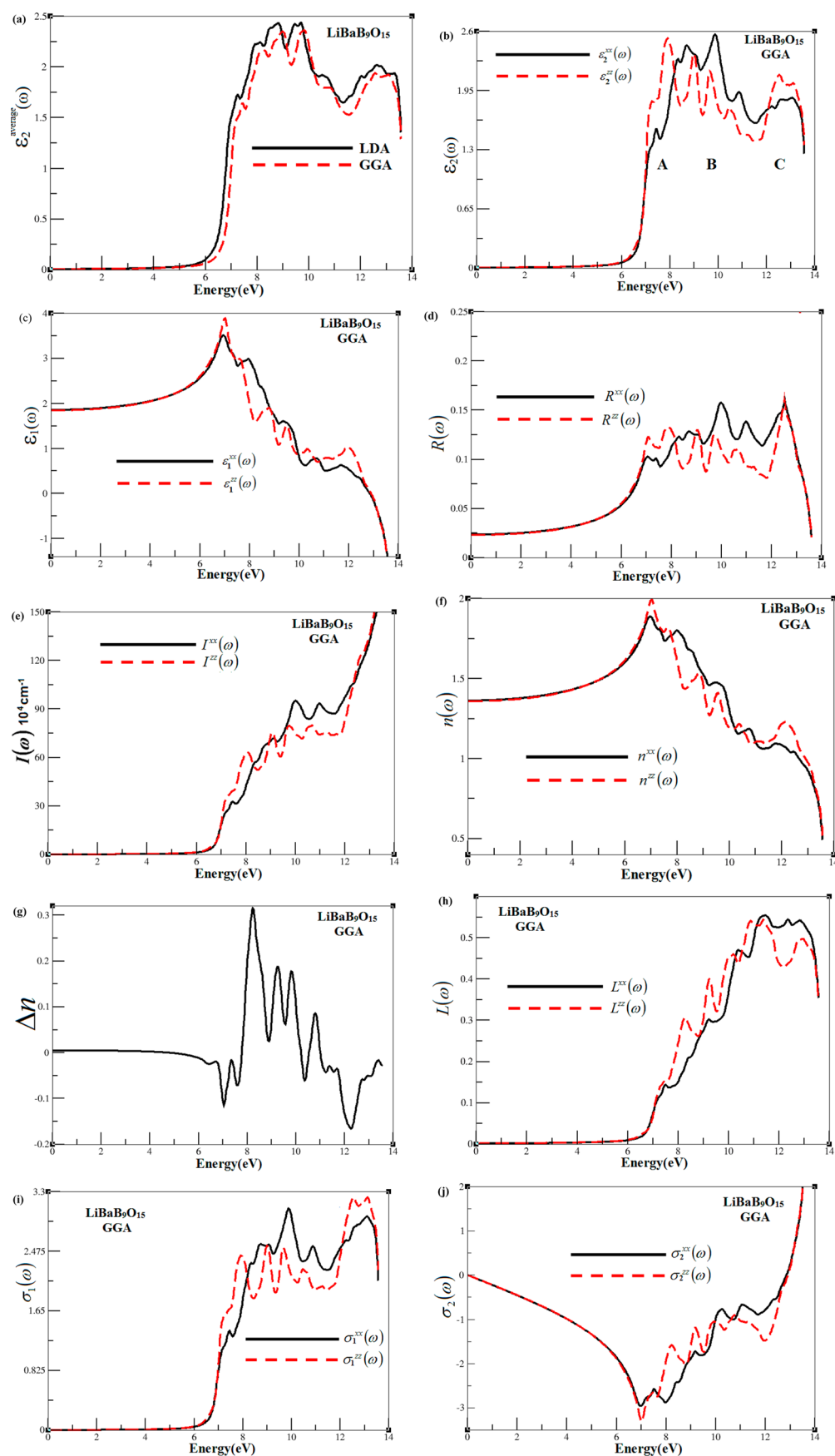
Figure 6. (a) Calculated $\varepsilon_2^{average}(\omega)$ using LDA and GGA with scissors corrections. (b) Calculated $\varepsilon_2^{xx}(\omega)$ (black, dark solid curve), $\varepsilon_2^{zz}(\omega)$ (red, light dashed curve) spectra using GGA with scissors correction. (c) Calculated $\varepsilon_1^{xx}(\omega)$ (black, dark solid curve), ε_1^{zz} (red, light dashed curve) spectra using GGA with scissors correction. (d) Calculated $R^{xx}(\omega)$ (black, dark solid curve), $R^{zz}(\omega)$ (red, light dashed curve), using GGA with scissors

Figure 6. continued

correction. (e) Calculated absorption coefficient $I^{xx}(\omega)$ (black, dark solid curve), $I^{zz}(\omega)$ (red, light dashed curve) spectrum using GGA with scissors correction, the absorption coefficient in 10^4 cm^{-1}. (f) Calculated refractive indices $n^{xx}(\omega)$ (black, dark solid curve), $n^{zz}(\omega)$ (red, light dashed curve) spectrum using GGA with scissors correction. (g) the calculated birefringence $\Delta n(\omega)$. (h) Calculated refractive indices $L^{xx}(\omega)$ (black, dark solid curve), $L^{zz}(\omega)$ (red, light dashed curve) spectrum using GGA with scissors correction. (i) Calculated refractive indices $\sigma_1^{xx}(\omega)$ (black, dark solid curve), $\sigma_1^{zz}(\omega)$ (red, light dashed curve) spectrum using GGA with scissors correction. (j) Calculated refractive indices $\sigma_2^{xx}(\omega)$ (black, dark solid curve), $\sigma_2^{zz}(\omega)$ (red, light dashed curve) spectrum using GGA with scissors correction.

spectral range between 0.0 and 8.0 eV, the B transitions are responsible for the structures of $\varepsilon_2^{xx}(\omega)$ and $\varepsilon_2^{zz}(\omega)$ in the spectral range between 8.0 and 10.0 eV, and the C transitions are responsible for the structures of $\varepsilon_2^{xx}(\omega)$ and $\varepsilon_2^{zz}(\omega)$ in the spectral range between 10.0 and 13.0 eV.

From the imaginary part of the dielectric function's dispersions $\varepsilon_2^{xx}(\omega)$ and $\varepsilon_2^{zz}(\omega)$, the real parts $\varepsilon_1^{xx}(\omega)$ and $\varepsilon_1^{zz}(\omega)$ were calculated using Kramers–Kronig relations.[22] The results of the calculated $\varepsilon_1^{xx}(\omega)$ and $\varepsilon_1^{zz}(\omega)$ are shown in Figure 6c. The calculated $\varepsilon_1^{xx}(0)$ and $\varepsilon_1^{zz}(0)$ (at the static limit) are presented in Table 1. Using the calculated dispersions of the imaginary and the real parts of the dielectric function, one can evaluate other optical properties such as reflectivity spectra $R(\omega)$, absorption coefficients $I(\omega)$, refractive indices $n(\omega)$, loss function $L(\omega)$, and the conductivity $\sigma(\omega)$. We show these quantities in Figure 6d–j. In Figure 6d, we show the calculated reflectivity spectra. Interestingly, there is an abrupt reduction in the reflectivity spectrum at 12.5 eV, confirming the occurrence of a collective plasmon resonance. The depth of the plasmon minimum is determined by the imaginary part of the dielectric function at the plasma resonance and is representative of the degree of overlap between the interband absorption regions. The calculated absorption coefficient dispersion $I(\omega)$ is shown in Figure 6e. At higher energies (at around 12.5 eV), this crystal shows a rapidly increasing absorption. The calculated refractive index dispersions $n(\omega)$ are shown in Figure 6f. The calculated values of $n^{xx}(0)$ and $n^{zz}(0)$ are listed in Table 1. Note that at low energy the LiBaB$_9$O$_{15}$ single crystal shows high refractive indices, which decrease at higher energies. The birefringence is the difference between the extraordinary and ordinary refraction indices, $\Delta n(\omega) = n_e(\omega) - n_o(\omega)$, where $n_o(\omega)$ is the index of refraction for an electric field oriented along the c-axis, and $n_e(\omega)$ is the index of refraction for an electric field perpendicular to the c-axis. Figure 6g shows the birefringence $\Delta n(\omega)$ dispersion for this single crystal. Clearly, the birefringence is important only in the nonabsorbing spectral range, which is below the energy gap. We find that the LiBaB$_9$O$_{15}$ single crystal possesses a positive birefringence at zero energy and at 1.165 eV (1064 nm) (see Table 1).

Electron energy loss spectroscopy (EELS) is a valuable tool for investigating various aspects of materials.[23] The plasmon losses corresponding to a collective oscillation of the valence electrons and their energies are related to the density of the valence electrons. In the case of interband transitions, which consist mostly of plasmon excitations, the scattering probability for the volume losses is directly connected to the energy loss function. In Figure 6h, the energy loss function is plotted in the basal-plane and in the direction of the c-axis. There are other features in this spectrum, in addition to the plasmon peak, associated with the interband transitions. The plasmon peak is usually the most intense feature in the spectrum; it appears at the energy at which $\varepsilon_1(\omega)$ goes to zero. The energy of the maximum peak of $(-\varepsilon_1(\omega))^{-1}$ is observed at ~12.5 eV for $L^{xx}(\omega)$ and $L^{zz}(\omega)$, which are assigned to the energy of the volume plasmon $\hbar\omega_p$. The calculated optical conductivity dispersion Im $\sigma(\omega)$ and Re $\sigma(\omega)$ are shown in Figure 6i,j, which also shows anisotropy between $\sigma^{xx}(\omega)$ and $\sigma^{zz}(\omega)$. The optical conductivity (OC) is related to the frequency-dependent dielectric function $\varepsilon(\omega)$ as $\varepsilon(\omega) = 1 + 4\pi i\sigma(\omega)/\omega$. The peaks in the optical conductivity spectra are determined by the electric-dipole transitions between the occupied states and the unoccupied states.

4.3. Nonlinear Optical Dispersion. Usually, calculating the nonlinear optical properties is much more complicated than calculating the linear ones. The difficulties concern both the numerical and the physical, because more conduction bands and more k-points are required to achieve the maximum accuracy. Since the investigated crystal belongs to the trigonal structure space group $R3c$, which possesses two crystallographic symmetry elements, we have, as a consequence, several parameters which are equal to zero. As a result the symmetry allows only three nonzero components, namely, the 113, 311, and 333 components (1, 2, and 3 refer to the x, y and z axes, respectively).[24] The complex second-order nonlinear optical susceptibility tensor $\chi_{ijk}^{(2)}(-2\omega;\omega;\omega)$ can be generally written as $\chi_{ijk}^{(2)}(\omega)$. The subscripts i, j, and k are the Cartesian indices. Accordingly, the LiBaB$_9$O$_{15}$ single crystal possesses the $\chi_{113}^{(2)}(\omega)$, $\chi_{311}^{(2)}(\omega)$, and $\chi_{333}^{(2)}(\omega)$ complex second-order nonlinear optical susceptibility tensors. The second-order nonlinear optical susceptibility is very sensitive to the scissors' correction. The scissors' correction has a profound effect on the magnitude and sign of $\chi_{ijk}^{(2)}(\omega)$.[25,26] The well known LDA and GGA underestimation of the energy band gaps may result in incorrect values of the second-order nonlinear optical susceptibility tensor components since they are more sensitive to the band gaps than the linear-response values due to the higher-power energy differences in the denominators of the formulas of complex second-order nonlinear optical susceptibility tensors given in refs 18, 27, and 28. In order to overcome this drawback a scissors' correction was used. It is well known that the nonlinear optical properties are more sensitive to small changes in the band structure than are the linear optical properties. Hence, any anisotropy in the linear optical properties is enhanced in the nonlinear spectra. This is attributed to the fact that the second harmonic response $\chi_{ijk}^{(2)}(\omega)$ involves the 2ω resonance in addition to the usual ω resonance. Both the ω and 2ω resonances can be further

Table 1. Calculated $\varepsilon_1^{xx}(\omega)$, $\varepsilon_1^{zz}(\omega)$, $n^{xx}(\omega)$, $n^{zz}(\omega)$, and $\Delta n(\omega)$ at Static Limit and at $\lambda = 1064$ nm

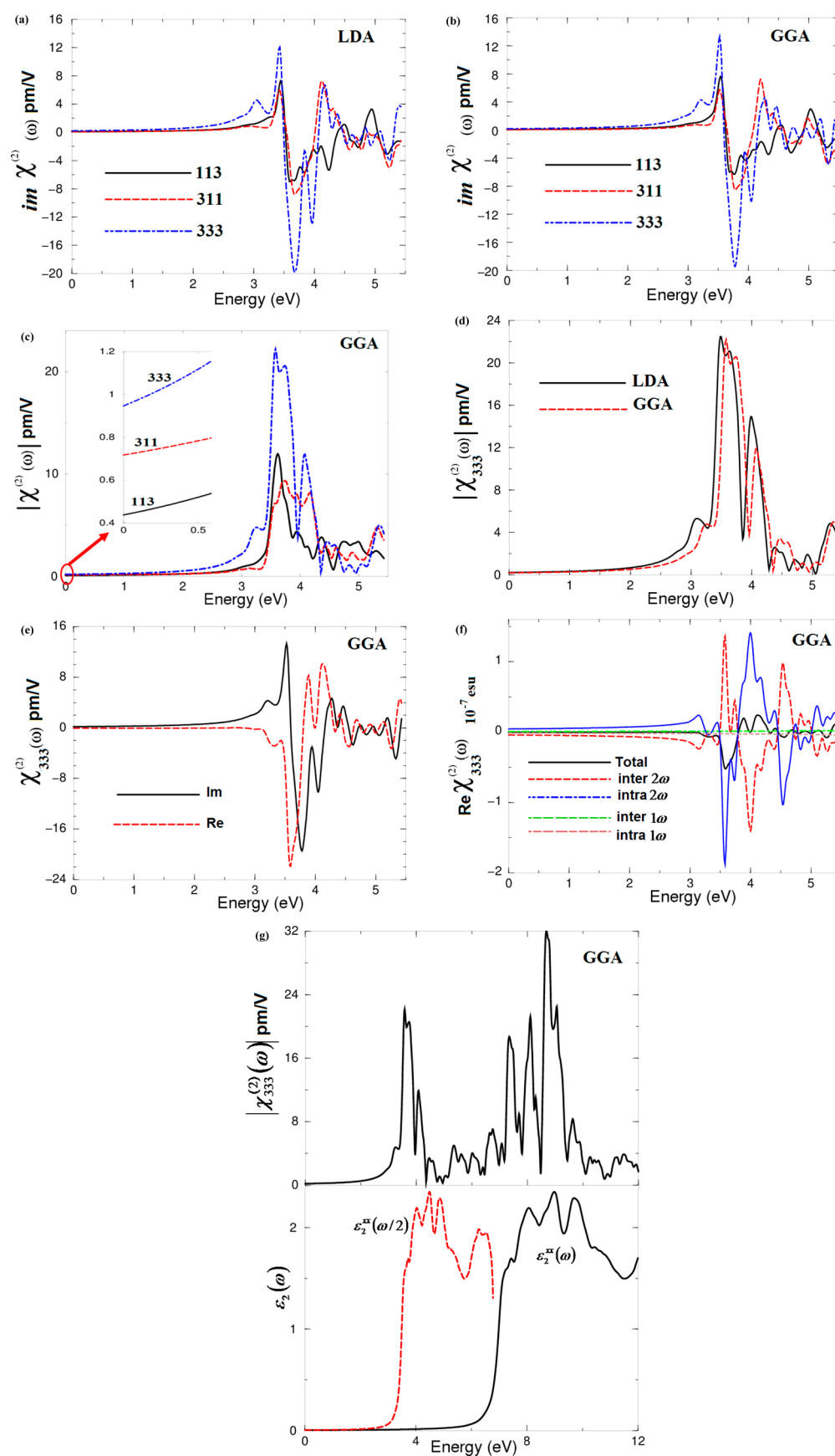|	theoretical at static limit	theoretical at $\lambda = 1064$ nm
$\varepsilon_1^{xx}(\omega)$	1.855	1.868
$\varepsilon_1^{zz}(\omega)$	1.842	1.856
$n^{xx}(\omega)$	1.362	1.367
n^{zz}	1.375	1.362
$\Delta n(\omega)$	0.003	0.002

Figure 7. (a) Calculated imaginary part for the three components using LDA with scissors correction. (b) Calculated imaginary part for the three components using GGA with scissors correction. (c) Calculated $|\chi^{(2)}_{ijk}(\omega)|$ for the three components using GGA with scissors correction. (d) Calculated $|\chi^{(2)}_{333}(\omega)|$ using LDA and GGA with scissors correction. (e) Calculated Imaginary part of $\chi^{(2)}_{333}(\omega)$ (black, dark solid curve) and real part of

Figure 7. continued

$\chi^{(2)}_{333}(\omega)$ (red, light dashed curve) spectra, using GGA with scissors correction. (f) Calculated total Re $\chi^{(2)}_{333}(\omega)$ spectrum (black, dark solid curve) along with the intra $(2\omega)/(1\omega)$ (blue, light solid curve)/(cyan, light dashed dotted curve) and inter $(2\omega)/(1\omega)$ (red, light long dashed curve)/ (green, light dotted curve)-band contributions; here all Re $\chi^{(2)}_{333}(\omega)$ are multiplied by 10^{-7}, in esu units. (g) (upper panel) Calculated $|\chi^{(2)}_{333}(\omega)|$ (black, dark solid curve) using GGA with scissors correction; (lower panel) calculated $\varepsilon^{xx}_2(\omega)$ (black, dark solid curve); calculated $\varepsilon^{xx}_2(\omega/2)$ (red, dark dashed curve).

Table 2. Calculated $|\chi^{(2)}_{ijk}(\omega)|$ in pm/V at Static Limit and at λ = 1064 nm along with the Values of d_{ijk}[a]

tensor components	theory $\chi^{(2)}_{ijk}(\omega)$ in (pm/V)	theory $d_{ijk} = 0.5\,\chi^{(2)}_{ijk}(\omega)$ in (pm/V)	theory $\chi^{(2)}_{ijk}(\omega)$ in (pm/V) at λ = 1064 nm	theory $d_{ijk} = 0.5\,\chi^{(2)}_{ijk}(\omega)$ in (pm/V) at λ = 1064 nm	exp d_{ijk} in (pm/V) at λ = 1064 nm
$|\chi^{(2)}_{113}(\omega)|$	0.44	d_{15} = 0.22	0.6	0.3	
$|\chi^{(2)}_{311}(\omega)|$	0.71	d_{31} = 0.35	0.79	0.39	0.45
$|\chi^{(2)}_{333}(\omega)|$	0.95	d_{33} = 0.47	1.5	0.75	1.21

[a]1 pm/V = 2.387×10^{-9} esu.

separated into interband and intraband contributions. The imaginary parts of the second harmonic generation susceptibility $\chi^{(2)}_{113}(\omega)$, $\chi^{(2)}_{311}(\omega)$, and $\chi^{(2)}_{333}(\omega)$ were calculated using the LDA and GGA as shown in Figure 7a,b. A definite enhancement in the anisotropy on going from the linear optical properties to the nonlinear optical properties is evident (see Figure 7a,b). We can identify the origin of the spectral peaks in these figures as being caused by $2\omega/\omega$ resonance peaks in the linear dielectric function. Figure 7c shows the calculated $|\chi^{(2)}_{ijk}(\omega)|$ for all components. Following this figure one can see that the calculated $|\chi^{(2)}_{ijk}(\omega)|$ components show that $|\chi^{(2)}_{333}(\omega)|$ is the dominant component. In Figure 7d we illustrated the dominant component calculated by the LDA and the GGA. In addition, we calculated the real and imaginary parts of the dominant component as illustrated by Figure 7e. In Figure 7f, we show the $2\omega/\omega$ inter/intra-band contributions to the total Im $|\chi^{(2)}_{333}(\omega)|$ of the dominant component $|\chi^{(2)}_{333}(\omega)|$. It is clear that the imaginary part of the second harmonic generation susceptibility is zero below half the energy band gap. The 2ω terms begin to contribute at energies ~1/2 E_g (2.585 eV), and the ω terms contribute at energy values above E_g. At low spectral range (≤2.585 eV) the SHG optical spectrum is dominated by the 2ω contributions. Beyond 5.17 eV (the values of the fundamental energy gaps) the major contribution comes from the ω term.

One would expect that the spectral structures in Im $\chi^{(2)}_{ijk}(\omega)$ could be understood from the structures in $\varepsilon_2(\omega)$. Unlike the linear optical spectra, the features in the SHG susceptibility are more difficult to identify from the band structure, because of the presence of 2ω and ω terms. But we can make use of the linear optical spectra to identify the different resonance leading to various features in the SHG spectra. The first structure in Im $\chi^{(2)}_{333}(\omega)$, between 2.59 and 5.17 eV, primarily originates from 2ω resonance and arises from the first structure in $\varepsilon_2(\omega)$. The second structure, between 5.17 and 10.0 eV, is associated with interference between ω resonance and 2ω resonance and associated with high structure in $\varepsilon_2(\omega)$. The last structure, from 10.0 to 14.0 eV, is mainly due to ω resonance and is associated with the tail in $\varepsilon_2(\omega)$. To analyze the features of the calculated $\chi^{(2)}_{113}(\omega)$, $\chi^{(2)}_{311}(\omega)$, and $\chi^{(2)}_{333}(\omega)$ spectra, it would be worthwhile to compare the absolute value of the dominant component $|\chi^{(2)}_{333}(\omega)|$ (Figure 7g, upper panel) with the absorptive part of the corresponding dielectric function $\varepsilon_2(\omega)$ as a function of both $\omega/2$ and ω (Figure 7g, lower panel). The first structure, $|\chi^{(2)}_{333}(\omega)|$, between 2.59 and 5.17 eV, is mainly originated from 2ω resonance [see $\varepsilon_2(\omega/2)$, Figure 7g, lower panel]. The

second structure, between 5.17 and 7.0 eV, is associated with interference between 2ω and ω resonances (the threshold of $\varepsilon_2(\omega)$) [see $\varepsilon_2(\omega/2)$ and $\varepsilon_2(\omega)$, Figure 7g, lower panel]. The last spectral structure (within the range 7.0−12.0 eV) is mainly due to ω resonance and is associated with the second structure in $\varepsilon_2(\omega)$. The calculated $|\chi^{(2)}_{ijk}(\omega)|$ values at zero limit and at λ = 1064 nm for all components are listed in Table 2. It is well known that the relationship between the second harmonic susceptibility coefficient d and the nonlinear susceptibility is $\chi^{(2)}_{ijk}(\omega) = 2d_{ijk} = d_{ij}$[24,29] (here i takes the values of 1, 2, and 3 corresponding to x, y, and z, and j takes the values of 1, 2, 3, 4, 5, and 6 corresponding to the xx, yy, zz, yz, xz, and xy components; for example, xx takes the value of 1, yy takes 2, zz takes 3, and so on). On the basis of this expression, we can obtain the values of d_{15}, d_{31}, and d_{33} from our calculated $|\chi^{(2)}_{ijk}(\omega)|$ at zero limit and at λ = 1064 nm. The calculated values of d_{15}, d_{31}, and d_{33} can be compared with our values measured using a Nd:YAG laser operating at 1064 nm; these values are listed in Table 2.

The microscopic first hyperpolarizability vector component, β_{333}, along the principal dipole moment direction for the $\chi^{(2)}_{333}(\omega)$ component, was obtained using the expression ($\beta_{ijk} = (\chi^{(2)}_{ijk})/(Nf^3)$), given in refs 24 and 30, where N is the number of molecules/cm^3 and f is the local field factor; the value of f varies between 1.3 and 2.0. Using this information we can estimate the value of the first hyperpolarizability tensor β_{ijk}. We have found that β_{333} is 0.186×10^{-30} esu at the static limit and 0.291×10^{-30} esu at λ = 1064 nm. We should emphasize that the last value shows good agreement with our measured one (0.467×10^{-30} esu) using a Nd:YAG laser operating at 1064 nm. In the LiBaB$_9$O$_{15}$ single crystal the microscopic first hyperpolarizability terms, β_{ijk}, cumulatively yield a bulk observable second order susceptibility term, $\chi^{(2)}_{ijk}(\omega)$, which in turn is responsible for the high SHG response of the LiBaB$_9$O$_{15}$ single crystal.

In order to justify its possible application as a nonlinear optical material we can compare this value with the calculated and measured value (31.6×10^{-30} esu at λ = 1064 nm) of the dominant component ($|\chi^{(2)}_{333}(\omega)|$ with d_{33} = 16.65 pm/V) of potassium titanyl phosphate KTiOPO$_4$ (KTP),[20] the well-known nonlinear optical single crystal that is commonly used for frequency doubling diode pumped solid-state lasers such as Nd:YAG and other neodymium-doped lasers. We believe that this work opens up the novel possibilities of interpreting the obtained optical functions of organic and inorganic materials and knowing the partial contributions of molecular groups. On

Table 3. Calculated and Measured d_{ijk} of LiBaB$_9$O$_{15}$ in Comparsion with the Available Experimental (Exp) and Theoretical (Theor) Results of LiB$_3$O$_5$ and β-BaB$_2$O$_4$ in pm/V at λ=1064 nm

LiBaB$_9$O$_{15}$		LiB$_3$O$_5$		β-BaB$_2$O$_4$	
exp (this work)	theor (this work)	exp[a]	theor[b]	exp	theor[e]
d_{15} =	d_{15} = 0.22	d_{32} = ± 0.85	d_{32} = 0.582	d_{22} = ± 1.6 (1 ± 0.05)[c] d_{22} = ± 2.2 (1 ± 0.05)[d]	d_{22} = −2.98
d_{31} = 0.45	d_{31} = 0.35	d_{31} = ± 0.67	d_{31} = −0.505	d_{31} = ±(0.11 ± 0.05)[c]	d_{31} = 0.18
d_{33} = 1.21	d_{33} = 0.47	d_{33} = ± 0.04	d_{33} = 0.014	d_{33} ≈ 0	d_{33} = 0.021

[a]Reference 31. [b]Reference 32. [c]Reference 5. [d]Reference 33. [e]Reference 34.

the other hand, when we compare the SHG of the LiBaB$_9$O$_{15}$ single crystal (approaching 1.21 pm/V) with that of KTP, we find the SHG of KTP to be larger than that of the LiBaB$_9$O$_{15}$ single crystal by about a factor of 13.

Finally we have compared our calculated and measured values of the SHG for LiBaB$_9$O$_{15}$ with the available experimental and theoretical results of the SHG for LiB$_3$O$_5$ and β-BaB$_2$O$_4$[5,31−34], as presented in Table 3. We should emphasize that the d_{33} of LiBaB$_9$O$_{15}$ is much bigger than that of LiB$_3$O$_5$ and of β-BaB$_2$O$_4$. Whereas the experimental value of d_{31} for LiBaB$_9$O$_{15}$ shows a reasonable agreement with that of LiB$_3$O$_5$, it is four times bigger than that of β-BaB$_2$O$_4$.

5. CONCLUSION

In this work, the synthesis and crystal structure of the noncentro-symmetric borate, LiBaB$_9$O$_{15}$, is reported. The compound possesses a three-dimensional $^3_\infty$[B$_9$O$_{15}$]$^{3−}$ anionic network, with one-dimensional channels occupied by Li$^+$ and Ba^{2+} cations. The basic structural unit in LiBaB$_9$O$_{15}$ is a [B$_3$O$_7$]$^{5−}$ group that consists of one BO$_4$ tetrahedron and two BO$_3$ triangles. The $^3_\infty$[B$_9$O$_{15}$]$^{3−}$ network is built up from the [B$_3$O$_7$]$^{5−}$ groups sharing all of the terminal O atoms. The UV−vis absorption spectrum has been investigated, and the optical band gap obtained by extrapolation of a linear-like absorption edge was roughly 5.17 eV, which is consistent with the observed color of the sample. We have performed a DFT calculation within the framework of the state-of-the-art all-electron full potential linearized augmented plane wave (FP-LAPW) method with different possible approximation for the exchange correlation (XC) potentials. We started the calculations by minimizing the forces (1 mRy/au) acting on each atom to optimize the atomic positions which are taken from our measured X-ray data (Supporting Information, CSD No. 426537). This calculation shows an energy gap of about 5.11 eV, in good agreement with the measured one. From the relaxed geometry the linear and nonlinear optical susceptibilities were calculated and compared with the experimental results, and good agreement was found. From the calculated and measured SHG the first hyperpolarizability was obtained.

ASSOCIATED CONTENT

Ⓢ Supporting Information

Crystallographic data obtained by X-ray measurements of the LiBaB$_9$O$_{15}$ single crystal. This material is available free of charge via the Internet at http://pubs.acs.org.

AUTHOR INFORMATION

Corresponding Author

*E-mail: maalidph@yahoo.co.uk. Tel.: +420 777 729 583. Fax: +420-386 361 219.

REFERENCES

(1) Becker, P. Borate Materials in Nonlinear Optics. *Adv. Mater.* **1998**, *10*, 979−992.

(2) Lin, Z.-B.; Hu, Z.-S.; Wang, G.-F. Growth and Characterization γ-Nd$_3$+:LaSc$_3$(BO$_3$)$_4$ Crystal. *Chin. J. Struct. Chem.* **2001**, *20*, 256−258.

(3) Pan, S.-K.; Wang, G.-F.; Huang, Z.-X. Synthesis and Structure of Ba$_3$La$_2$(BO$_3$)$_4$ Crystal. *Chin. J. Struct. Chem.* **2002**, *21*, 382−384.

(4) Chen, C. T.; Wu, Y.; Jiang, A.; Wu, B.; You, G.; Li, R.; Lin, S. New Nonlinear-Optical Crystal: LiB$_3$O$_5$. *J. Opt. Soc. Am. B* **1989**, *6*, 616−621.

(5) Chen, C. T.; Wu, B.; Jiang, A.; You, G. A New Type of Ultraviolet SHG Crystal: β-BBO. *Sci. China, B* **1985**, *18*, 235−243.

(6) Cheng, W.-D.; Zhang, H.; Lin, Q.-S.; Zheng, F.-K.; Chen, J.-T. Syntheses, Crystal and Electronic Structures, and Linear Optics of LiMBO$_3$(M = Sr, Ba) Orthoborates. *Chem. Mater.* **2001**, *13*, 1841−1847.

(7) Huang, Q.; Lu, S.; Dai, G.; Liang, J. A New Type of Borate Double Salt: Structure of LiBa$_2$B$_5$O$_{10}$. *Acta Crystallogr., Sect. C: Crsyt. Struct. Commun.* **1992**, *48*, 1576−1578.

(8) Penin, N.; Seguin, L.; Touboul, M.; Nowogrocki, G. Synthesis and Crystal Structure of Three MM′B$_9$O$_{15}$ Borates (M = Ba, Sr and M′ = Li; M = Ba and M′ = Na). *Int. J. Inorg. Mater.* **2001**, *3*, 1015−23.

(9) Pushcharovsky, D. Y.; Gobetchia, E. R.; Pasero, M.; Merlino, S.; Dimitrova, O. V. Hydrothermal Synthesis and Crystal Structures of Li,Ba-Nanoborate, LiBaB$_9$O$_{15}$, and Ba-Borophosphate, BaBPO$_5$. *J. Alloys Compd.* **2002**, *339*, 70−75.

(10) Sheldrick, G. M. *SHELX-97: Program for Structure Refinement*; University of Goettingen: Germany, 1997.

(11) Christ, C. L.; Clark, J. R. A Crystal-Chemical Classification of Borate Structures with Emphasis on Hydrated Borates. *Phys. Chem. Miner.* **1977**, *2*, 59−87.

(12) Heller, G. A Survey of Structural Types of Borates and Polyborates. *Top. Curr. Chem.* **1986**, *131*, 39−98.

(13) Kolev, Ts.; Kityk, I. V.; Ebothe, J.; Sahraoui, B. Intrinsic Hyperpolarizability of 3-Dicyanomethylene-5,5-dimethyl-1-[2-(4-hydroxyphenyl)ethenyl]-cyclohexene Nanocrystallites Incorporated into the Photopolymer Matrices. *Chem. Phys. Lett.* **2007**, *443*, 309−312.

(14) Blaha, P.; Schwarz, K.; Madsen, G. K. H.; Kvasnicka, D.; Luitz, J. *WIEN2K, An Augmented Plane Wave + Local Orbitals Program for Calculating Crystal Properties*; Karlheinz Schwarz, Technische Universitat: Wien, Austria, 2001, ISBN: 3-9501031-1-2.

(15) Hohenberg, P.; Kohn, W. Inhomogeneous Electron Gas. *Phys. Rev. B* **1964**, *136*, 864−871.

(16) Ceperley, D. M.; Ader, B. I. Ground State of the Electron Gas by a Stochastic Method. *Phys. Rev. Lett.* **1980**, *45*, 566−569. (b) Perdew, J. P.; Zunger, A. One-Electron Theory of the Bulk Properties of Crystalline Ar, Kr, and Xe. *Phys. Rev. B* **1973**, *8*, 4822−4832.

(17) Perdew, J. P.; Burke, S.; Ernzerhof, M. Generalized Gradient Approximation Made Simple. *Phys. Rev. Lett.* **1996**, *77*, 3865−3868.

(18) Reshak, A. H.; Stys, D.; Auluck, S.; Kityk, I. V. Density Functional Calculations of the Electronic Structure of 3-Phenylamino-4-phenyl-1,2,4-triazole-5-thione. *Phys. Chem. Chem. Phys.* **2010**, *12*, 2975−2980.

(19) Reshak, A. H.; Stys, D.; Auluck, S.; Kityk, I. V. Linear and Nonlinear Optical Susceptibilities of 3-Phenylamino-4-phenyl-1,2,4-triazole-5-thione. *J. Phys. Chem. B* **2010**, *114*, 1815−1821.

(20) Reshak, A. H.; Kityk, I. V.; Auluck, S. Investigation of the Linear and Nonlinear Optical Susceptibilities of $KTiOPO_4$ Single Crystals: Theory and Experiment. *J. Phys. Chem B* **2010**, *114* (50), 16705−16712.

(21) (a) Sergey, N. R.; Walter, R. L. L. Second-Harmonic Generation of I-III-VI2 Chalcopyrite Semiconductors: Effects of Chemical Substitutions. *Phys. Rev. B* **2001**, *63*, 165212−1652024. (b) Sergey, N. R.; Walter, R. L. L.; Segall, B. Efficient Ab Initio Method for the Calculation of Frequency-Dependent Second-Order Optical Response in Semiconductors. *Phys. Rev. B* **1998**, *57*, 3905−3919. (c) Reshak, A. H.; Kamarudin, H.; Auluck, S. Dispersion of the Linear and Nonlinear Optical Susceptibilities of Disilver Germanium Sulfide from DFT Calculations. *J. Mater. Sci.* **2013**, *48*, 1955−1965. (d) Reshak, A. H.; Stys, D.; Auluck, S.; Kityk, I. V. Dispersion of Linear and Nonlinear Optical Susceptibilities and the Hyperpolarizability of 3-Methyl-4-phenyl-5-(2-pyridyl)-1,2,4-triazole. *Phys. Chem. Chem. Phys.* **2011**, *13*, 2945−2952. (e) Reshak, A. H.; Auluck, S.; Stys, D.; Kityk, I. V.; Kamarudin, H.; Berdowski, J.; Tylczynski, Z. Dispersion of Linear and Non-Linear Optical Susceptibilities for Amino Acid 2-Aminopropanoic $CH_3CH(NH_2)COOH$ Single Crystals: Experimental and Theoretical Investigations. *J. Mater. Chem.* **2011**, *21*, 17219−17228.

(22) Wooten, F. 1972 *Optical Properties of Solids*; Academic Press: New York.

(23) Loughin, S.; French, R. H.; De Noyer, L. K.; Ching, W.-Y.; Xu, Y.-N. J. Critical Point Analysis of the Interband Transition Strength of Electrons. *J. Phys. D: Appl. Phys.* **1996**, *29*, 1740−1750.

(24) Boyd, R. W. *Principles of Nonlinear Optics*; Academic Press: New York, 1982, p 420

(25) Reshak, A. H.; Auluck, S. Ab Initio Calculations of the Electronic, Linear and Nonlinear Optical Properties of Zinc Chalcogenides. *Phys. B* **2007**, *388*, 34−42.

(26) Reshak, A. H.; Auluck, S.; Kityk, I. V. Experimental and Theoretical Investigations of the First and Second Order Optical Susceptibilities of BiB_3O_6 Single Crystal. *Appl. Phys. A: Mater. Sci. Process.* **2008**, *91*, 451−457.

(27) Sharma, S.; Dewhurst, J. K.; Ambrosch-Draxl, C. Linear and Second-Order Optical Response of III-V Monolayer Superlattices. *Phys. Rev. B* **2003**, *67*, 165332−165341.

(28) Reshak, A. H. Ph.D. Thesis, Indian Institute of Technology-Rookee: India, 2005.

(29) *Nonlinear Polarization*. http://www.rp-photonics.com/nonlinear_polarization.html (accessed 2013).

(30) Boyd, R. W. *Nonlinear Optics*, 3rd ed.; Acadmic Press: Philadelphia, 2008, ISBN:978-0-12-369470-6.

(31) Dmitriev, V. G.; Gurzadyan, G. G.; Nikogosyan, D. N. *Handbook of Nonlinear Optical Crystals*; Springer: New York, 1995.

(32) Zheshuai, L.; Jiao, L.; Zhizhong, W.; Chuangtian, C. Mechanism for Linear and Nonlinear Optical Effects in LiB_3O_5, CsB_3O_5, and $CsLiB_6O_{10}$ Crystals. *Phys. Rev. B* **2000**, *62*, 1757−1764.

(33) Eckardt, R. C.; Masuda, H.; Fan, Y. X.; Byer, R. L. Absolute and Relative Nonlinear Optical Coefficients of KDP, KD*P, BaB_2O_4, $LiIO_3$, $MgO:LiNbO_3$, and KTP Measured by Phase-Matched Second-Harmonic Generation. *IEEE J. Quantum Electron.* **1990**, *26*, 922−933.

(34) Duan, C.-G.; Li, J.; Gu, Z.-Q.; Wang, D.-S. Interpretation of the Nonlinear Optical Susceptibility of Borate Crystals from First Principles. *Phys. Rev. B* **1999**, *59*, 369−372.

14150

dx.doi.org/10.1021/jp4077905 | *J. Phys. Chem. B* 2013, 117, 14141−14150